Modeling Internal Flow Through a Rotating Duct Using Quasi 1-D Euler Equations

Anand Karpatne* and Jayant Sirohi†
The University of Texas at Austin, Austin, Texas 78712

A numerical model of the internal flow in a duct rotating about one end is described. One-dimensional Euler equations are solved inside the duct using a finite volume formulation in which the advective fluxes are calculated using the advection upwind splitting method. The model was developed as a fast design tool for helicopter rotor blades with internal spanwise flow. To this end, centrifugal as well as Coriolis effects, frictional losses, duct sweep, and time-dependent duct boundary conditions are modeled, and a spanwise flow control valve can be included. The model is used to explore the behavior of a 2-m-long duct with a circular cross section, rotating at tip speeds of up to 260 m/s. The effects of centrifugal pumping, duct friction, duct sweep, and a flow control valve on the spanwise pressure and velocity distribution, mass flow rate of air through the duct, and torque required to spin the duct are discussed.

Nomenclature

a_{rel}	=	relative acceleration of the rotating reference frame with respect to inertial frame
F	=	flux vector (x direction)
F^C	=	inviscid flux vector due to convection (x direction)
F^D	=	diffusive flux vector (x direction)
F^I	=	inviscid flux vector (x direction)
F^P	=	pressure flux vector (x direction)
F_j	=	flux vector (x direction) across face "j"
G	=	flux vector (y direction)
G_j	=	flux vector (y direction) across face "j"
K	=	thermal conductivity of the medium, W/m · K
M	=	Mach number
P	=	local static pressure, Pa
$P_{1/2}$	=	local static pressure at a face denoted by (1/2), Pa
Q	=	vector of forcing/source terms
q	=	duct torque due to internal flow, N · m
R	=	length of the rotating duct, m
r_x	=	distance of any point from the axis of rotation in the x direction, m
r_y	=	distance of any point from the axis of rotation in the y direction, m
T	=	local static temperature, K
u	=	velocity of fluid in the x direction, m/s
v	=	velocity of the fluid in the y direction, m/s
w	=	velocity of a fluid element in the rotating reference frame
x	=	coordinate along duct axis, m
y	=	coordinate perpendicular to duct axis, m
Δt	=	computational time step, s
ΔV	=	volume of a unit cell, m³
Δx	=	spanwise length of each grid cell, m
Ω	=	rotational rate of the duct, rad/s
ρ	=	density of air, kg/m³

*Graduate Research Assistant, Department of Aerospace Engineering and Engineering Mechanics.
†Associate Professor, Department of Aerospace Engineering and Engineering Mechanics.

I. Introduction

THE understanding of flow inside a rotating duct is central to several rotorcraft applications such as circulation control (CC), tip jet-driven rotors, and pneumatically powered actuators. In CC rotors such as the Sikorsky X-wing [1] and tip jet-driven rotors such as the Boeing Canard Rotor Wing [2], a significant mass of air is pumped through the rotor blades. Recently, Szefi et al. [3] conducted experiments on pneumatic on-blade actuators powered by the pressure differential created by centrifugal pumping in ducts oriented along the rotor blade span. Drury et al. [4] performed full-scale tests on a rotor blade deicing system powered by centrifugal pumping. Proper design of the rotor blade for such applications, especially those relying purely on centrifugal pumping, requires detailed knowledge of the internal flow under a variety of time-varying boundary conditions.

There have been numerous studies on the simulation of internal flow in rotating ducts. Sophisticated computational fluid dynamics (CFD) models like RANS or DNS have been applied to simulate turbulent rotating channel flows [5–8]. Williams [9] developed one of the first analyses for internal flow in a CC rotor. The steady Navier–Stokes (N-S) equations were solved inside the rotor duct and the effects of CC on hover performance were obtained. The drawback of this method was its inability to capture transient flow physics inside the rotor blade. A RANS-based N-S solver was used to solve for external airflow over a CC wind turbine blade [10] and estimates of aerodynamic performance were made. Watkins et al. [11,12] developed a numerical formulation of the unsteady internal flow and correlated the results with experiments conducted on a reduced scale, nonrotating CC rotor blade. An implicit finite-difference method based on the Beam–Warming scheme was used for the numerical solution of 1-D N-S equations. The dissipative nature of the differencing scheme limited its ability to model shocks, thereby restricting its applicability only to subsonic flows. The effects of a varying inlet valve area on the internal flow features were also obtained. However, due to the nondimensionalization of the N-S equations by the duct cross-sectional area, a closed valve (with zero cross-sectional area) could not be modeled inside the duct.

The spanwise flow can have a profound effect not only on the aerodynamic behavior of the rotor blade, but also on the rotor torque and stability. For instance, Chopra [13] studied the effect of CC on the aeroelastic stability of flap bending, lead-lag bending, and torsion of a bearingless rotor in hover, and concluded that trailing edge blowing played a significant role in the stability of the rotor blade. It was observed that, at a fixed thrust level, increased blowing leads to aeroelastic instability.

In this paper, we discuss a numerical model that captures the key internal flow phenomena inside a rotating duct, without being as computationally expensive as full-scale CFD. For example, calculation of the steady-state flow through a rotating duct can be

accomplished in the order of minutes using the present model, in contrast to several hours using a commercial CFD solver. Therefore, the present model can be used as a design tool for rotor blades with centrifugally pumped spanwise flow. Quasi 1-D Euler equations are solved for a duct rotating about one end using a finite volume method, where the inviscid fluxes are modeled using an advection upwind splitting method (AUSM) scheme. The evolution of internal flow with time for various rotational speeds is studied. The effect of duct friction, duct sweep, and of a flow control valve at an arbitrary spanwise location and with an arbitrary time varying area is modeled. Additionally, the effect of duct flow on total rotor torque is obtained.

II.   Methodology

The methodology involves solving the quasi 1-D Euler equations inside a rotating duct. The term "quasi" is important because the formulation of the Euler equations itself is in 2-D, but the duct is discretized only along its length. A schematic of the rotor blade with a spanwise duct is shown in Fig. 1. The duct consists of a straight section, a transitional section, and a swept section to represent the geometry of a typical modern helicopter rotor blade. In the rotating reference frame (x-y as shown in the figure), the velocity of a fluid element with mass dm is shown as u and v. The conservative form of the continuity, momentum, and energy equation in this frame is given as

$$\frac{\partial U}{\partial t} + \frac{\partial F}{\partial x} + \frac{\partial G}{\partial y} = Q \tag{1}$$

where U is a vector containing all conservative variables, F and G contain the fluxes in the x and y directions, respectively, and Q contains all the forcing/source terms arising from the acceleration of an element dm due to the noninertial motion of the x-y frame. These vectors are

$$U = \left\{ \begin{array}{c} \rho \\ \rho u \\ \rho v \\ \rho E^* \end{array} \right\} \tag{2}$$

$$F = \left\{ \begin{array}{c} \rho u \\ \rho u^2 + P \\ \rho u v \\ \rho u \left(E^* + \frac{P}{\rho} \right) - K \frac{\partial T}{\partial x} \end{array} \right\} \tag{3}$$

$$G = \left\{ \begin{array}{c} \rho v \\ \rho u v \\ \rho v^2 + P \\ \rho v \left(E^* + \frac{P}{\rho} \right) - K \frac{\partial T}{\partial y} \end{array} \right\} \tag{4}$$

$$Q = \left\{ \begin{array}{c} 0 \\ 2\rho\Omega v + \Omega^2 \rho r_x \\ -2\rho\Omega v + \Omega^2 \rho r_y \\ 0 \end{array} \right\} \tag{5}$$

Here, E^* is the total energy of the system, given by

$$E^* = e + \frac{u^2 + v^2}{2} - \frac{\Omega^2 (r_x^2 + r_y^2)}{2} \tag{6}$$

where e is the internal energy per unit mass of the system, and r_x and r_y are the positions of the cell centers in the x and y directions, respectively.

The duct is discretized along its length into several elements with rectangular cross-sectional areas (Fig. 1). The geometric centers of each cell are shown in the figure (denoted as $i - 1$, i, $i + 1$). Equation (1) is solved at each cell center using the values of fluxes F and G through all the faces of that cell, while the values of Q are calculated at the cell centers. The AUSM upwind scheme, described by Liou and Steffen Jr. [14], is used to calculate the inviscid fluxes.

The total inviscid flux $F^I_{1/2}$ at an interface between two cells (denoted by $1/2$) is given by a summation of a convective flux $F^C_{1/2}$ and a pressure flux $F^P_{1/2}$. In addition to the inviscid flux, the diffusive flux $F^D_{1/2}$ that represents thermal diffusion through the interface is also considered [Eq. (7)]. A simple forward differencing is used to compute the temperature gradient across the face. Note that this flux does not include the effect of viscosity, which is handled separately by modeling duct friction

$$F^D_{1/2} = \left\{ \begin{array}{c} 0 \\ 0 \\ 0 \\ -K \frac{T_R - T_L}{X_R - X_L} \end{array} \right\} \tag{7}$$

The total flux $F_{1/2}$ through the interface can be represented as the summation of inviscid and diffusive fluxes

$$F_{1/2} = F^C_{1/2} + F^P_{1/2} + F^D_{1/2} \tag{8}$$

Matrices $\tilde{F}$ and $\tilde{G}$ that contain all the x and y fluxes through each of the four faces of a cell "i" can be written as

$$\tilde{F}_i = [F_1 F_2 F_3 F_4]_i \quad \tilde{G}_i = [G_1 G_2 G_3 G_4]_i \tag{9}$$

The area vector dS for a cell "i" corresponding to the four surrounding faces is given as
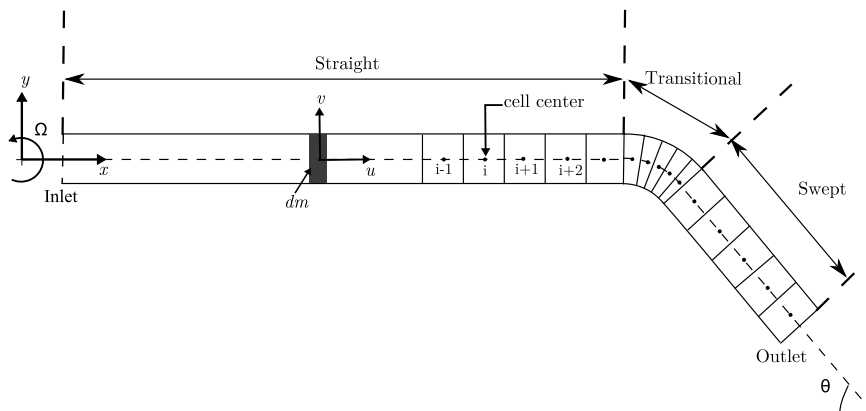

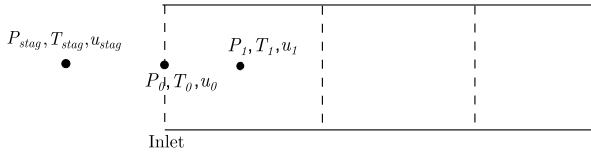**Fig. 1   Schematic of a rotating duct with spanwise discretization.**

Fig. 2 Open inlet configuration.

$$dS = \begin{Bmatrix} dS_1 \\ dS_2 \\ dS_3 \\ dS_4 \end{Bmatrix} \qquad (10)$$

At a time step "k," once the values of all fluxes and source terms for each cell "i" are known, Eq. (1) can be expanded in explicit form to obtain the solution at the "$(k + 1)$th" time step, U^{k+1}:

$$U_i^{k+1} = U_i^k - \frac{\Delta t}{\Delta V_i}(\tilde{F}dS \cdot \hat{e}_x)_i - \frac{\Delta t}{\Delta V_i}(\tilde{G}dS \cdot \hat{e}_y)_i + Q_i \Delta t \quad (11)$$

Here $\hat{e}_x$ and $\hat{e}_y$ represent the unit vectors pointing in the x and y directions, respectively.

A. Boundary Conditions

The correct implementation of boundary conditions at the inlet and outlet is crucial for accurate modeling of the duct flow. Implementation of various boundary conditions, representing both closed- and open-ended rotating ducts, is described below. A combination of isentropic flow theory and Riemann invariants is applied to obtain the necessary conditions. For a more refined analysis, it is possible to implement coupling between internal and external flows by specifying the pressure boundary conditions calculated by an external flow CFD solver.

1. Open Inlet

For an open inlet, the flow is assumed to enter the duct with stagnation conditions from a plenum (P_{stag}, T_{stag}). Because there is no nozzle at the inlet, the flow remains subsonic outside the inlet. When the inlet Mach number becomes equal to 1, the flow becomes choked.

It is well known that, for a subsonic inlet, two characteristic waves approach the boundary from the outside while one characteristic approaches it from the computational grid [15]. Therefore, to establish the boundary conditions, the information of isentropic flow expansion coming from the outside can be coupled with 1-D Riemann's invariant information coming from the interior grid points. The isentropic relationship between the stagnation temperature T_{stag} upstream from the inlet and the temperature at the boundary point T_0 is

$$T_{stag} = T_0 + \frac{(\gamma - 1)u_0^2}{2\gamma R} \qquad (12)$$

The Riemann invariants (R^-) are quantities that remain constant along the characteristic curves of 1-D Euler equations. Therefore, between points 0 and 1 (Fig. 2), (R^-) is constant and is given as

$$R_1^- = u_1 - \frac{2\sqrt{\gamma R T_1}}{\gamma - 1} \qquad (13a)$$

$$R_0^- = u_0 - \frac{2\sqrt{\gamma R T_0}}{\gamma - 1} \qquad (13b)$$

Equating R_0^- and R_1^- from Eq. (13), we get

$$u_0 = u_1 - \frac{2\sqrt{\gamma R T_1}}{\gamma - 1} + \frac{2\sqrt{\gamma R T_0}}{\gamma - 1} \qquad (14)$$

The values of T_0 and u_0 are evaluated iteratively using Eqs. (12) and (14). To start the process, a guess of T_0 is chosen as T_{stag} and u_0 is chosen as u_1, which is the value of spanwise velocity at the first grid point. Once T_0 and u_0 are known, the pressure P_0 is obtained using isentropic relations:

$$P_0 = P_{stag}\left(1 + \frac{\gamma - 1}{2}\frac{u_0^2}{\gamma R T_0}\right)^{-(\gamma/\gamma - 1)} \qquad (15)$$

2. Closed Inlet

For a closed inlet, the velocity at the inlet face is set to zero. The pressure P_0 at the inlet face is calculated from the 1-D characteristic relation between points 0 and 1 [Eq. (16)]

$$P_0 = P_1 - \rho u a_1 \qquad (16)$$

Here, P_1 is the pressure at the first grid point and u_1 is the velocity at the first grid point normal to the inlet face and pointing away from it. The temperature T_0 at the inlet face is obtained from isentropic relations [Eq. (17)]

$$T_0 = T_1 + \frac{(\gamma - 1)u_1^2}{2\gamma R} \qquad (17)$$

3. Open Outlet

Two cases, corresponding to a subsonic and supersonic outlet, are discussed below. For a subsonic outlet, pressure at the exit is specified, while for a supersonic outlet, the exit boundary conditions are extrapolated from inside the computational domain.

Subsonic: At the outlet, for a subsonic case, two of the primitive variables (P, ρ, u) are obtained from inside the computational domain, while one value is specified at the exit [15]. In the current simulation, the external pressure is specified (P_{atm}) and the density ρ_e, exit velocity normal to the outlet face u_e, and the outlet temperature T_e are obtained from a combination of 1-D normal characteristic equations [15] and the ideal gas law [Eq. (18)]. Here, "n" is the index of the last computational grid point and "e" denotes the duct exit

$$\rho_e = \frac{\rho_n}{(1 - P_e - P_n/\gamma P_e)} \qquad (18a)$$

$$T_e = \frac{P_e}{R\rho_n}\left(1 - \frac{P_e - P_n}{\gamma P_e}\right) \qquad (18b)$$

$$u_e = \frac{P_n - P_e}{\rho_e\sqrt{\gamma P_e/\rho_n(1 - P_e - P_n/\gamma P_e)}} + u_n \qquad (18c)$$

Supersonic: In the supersonic case, all the three wave characteristics travel in the outward direction toward the exit. Thus, the values of P_e, ρ_e, and u_e at the exit face are extrapolated from inside the domain using a zeroth-order approximation.

4. Closed Outlet

Similar to the closed inlet case, the exit value u_e is set to zero for the closed outlet. The outlet temperature T_e and pressure P_e are obtained from the 1-D characteristic equation [Eq. (19)]:

$$P_e = P_n + \rho u_n a_n \qquad (19)$$

where P_n is the pressure at the last computational grid point and u_n is the normal velocity at the last grid point pointing toward the exit. The

temperature T_e at the outlet face is estimated from the isentropic flow relation [Eq. (20)]:

$$T_e = T_n + \frac{(\gamma-1)u_n^2}{2\gamma R} \qquad (20)$$

B. Initial Conditions

The initial conditions are chosen equal to inlet plenum conditions for pressure, density, and temperature, while the initial duct rotational speed is set to zero. The duct is instantaneously given an angular velocity Ω at $t=0$ and the flow is allowed to evolve inside the duct.

C. Friction Forces

The effects of viscosity are included in the model by using a friction factor that relates the dynamic pressure of the flow to the wall shear stress. The Fanning friction factor is chosen based on the geometry of duct and the Reynolds number. It is defined using Churchill's approximation for turbulent flow [16]

$$f = 2\left[\left(\frac{8}{Re}\right)^{12} + (A+B)^{-1.5}\right]^{1/12} \qquad (21)$$

$$A = \left[2.457\, \ell n\left(\frac{1}{(7/Re)^{0.9}+0.27\epsilon/D}\right)\right]^{16} \qquad (22a)$$

$$B = \left(\frac{37530}{Re}\right)^{16} \qquad (22b)$$

where $Re = (\rho|u_n|D/\mu)$ is the Reynolds number based on the diameter D of the duct and the velocity u_n normal to the cross section of the duct, and ϵ is the surface roughness coefficient that reflects the smoothness of the internal surface of the duct. The wall shear stress τ_w is related to the friction factor by

$$\tau_w = f\frac{\rho u_n^2}{2} \qquad (23)$$

Using Eq. (23), the differential friction force per unit volume is

$$\frac{dF_{\text{friction}}}{dV} = \frac{2f\rho u_n^2}{D} \qquad (24)$$

In the present analysis, friction is modeled by including additional terms into the forcing vector Q as shown in Eq. (25). Note that, to accommodate the directionality of friction force (opposing velocity), $(u/|u|)$ is used to determine the direction of flow

$$Q = \begin{Bmatrix} 0 \\ 2\rho\Omega v + \Omega^2\rho r_x - \frac{2f\rho(u^2+v^2)}{D}\frac{u}{|u|} \\ -2\rho\Omega v + \Omega^2\rho r_y - \frac{2f\rho(u^2+v^2)}{D}\frac{v}{|v|} \\ -\left(2f\rho\frac{(u^2+v^2)}{D}\right)|u_n| \end{Bmatrix} \qquad (25)$$

D. Duct Sweep

As seen in Fig. 1, the duct is divided into three sections: straight, transitional, and swept. In the straight section, the cell centers are aligned with the x axis. In the transitional section, the angle made by the axis of the duct with the horizontal smoothly changes from 0 to the sweep angle θ. Therefore, every cell in this section is trapezoidal. Finally, for the swept section all cell faces are inclined at the sweep angle θ. A positive value of θ corresponds to backward swept duct and a negative value corresponds to forward sweep.

E. Flow Control Valve

The opening and closing of a flow control valve in the duct is modeled as a local change in the duct cross-sectional area. The spanwise discretization is performed such that a cell face coincides with the valve location. The area of this face can be changed as a function of time, simulating an arbitrary opening and closing of the valve. A schematic of the duct discretization including valve geometry is shown in Fig. 3.

Upon changing the valve area, the length of face "A" reduces. This causes the shape of the cells at "i" and "$i+1$" to change from perfectly rectangular to trapezoidal and the face unit normals (n_x and n_y) for faces "C" and "D" are appropriately adjusted. Subsequently, pressure fluxes through faces C and D, in both the spanwise and chordwise directions, are also considered. In this way, the fluxes through all the faces around the valve are altered. Note that a fully closed valve can be modeled by setting the length of face A equal to zero, resulting in triangular cells adjacent to the valve. In this situation, face A behaves like a closed boundary through which the convective flux $F_{1/2}^c$ is zero.

F. Rotor Torque

The flow through the duct results in a torque on the rotor blade due to spanwise Coriolis forces on the moving fluid as well as momentum changes at the inlet and efflux. To compute the torque applied q at the rotor hub due to internal flow, the moment of the integral inviscid momentum equation is taken [Eq. (26)]. The right-hand side of this equation is computed numerically at each time step. Note that this torque does not take external flow into consideration (e.g., profile drag and induced drag on the rotor blade). Therefore, it only corresponds to the incremental rotor torque due to duct flow

$$q = \Sigma r \times F$$
$$= \int_{CV} r \times \frac{\partial}{\partial t}(\rho w)\,dV + \int_{CS} r \times \rho w(w\cdot ds) + \int_{CV} r \times a_{\text{rel}}\,dm \qquad (26)$$

G. Time Stepping

An explicit fourth-order Runge–Kutta scheme is used to compute the values of the conservative variable vector U at every time step. Equation (1) is re-written as

$$\frac{\partial U}{\partial t} = f \qquad (27)$$

where $f = -(\partial F/\partial x) - (\partial G/\partial y) + Q$. To compute the time step Δt, the Courant–Friedrichs–Lewy number (based on tip speed) is heuristically chosen as 0.3 [Eq. (28)], assuming that the maximum
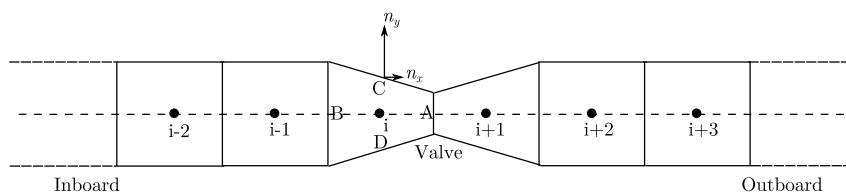
Fig. 3   Schematic showing the positioning of a valve inside the duct. Face A corresponds to the valve location.
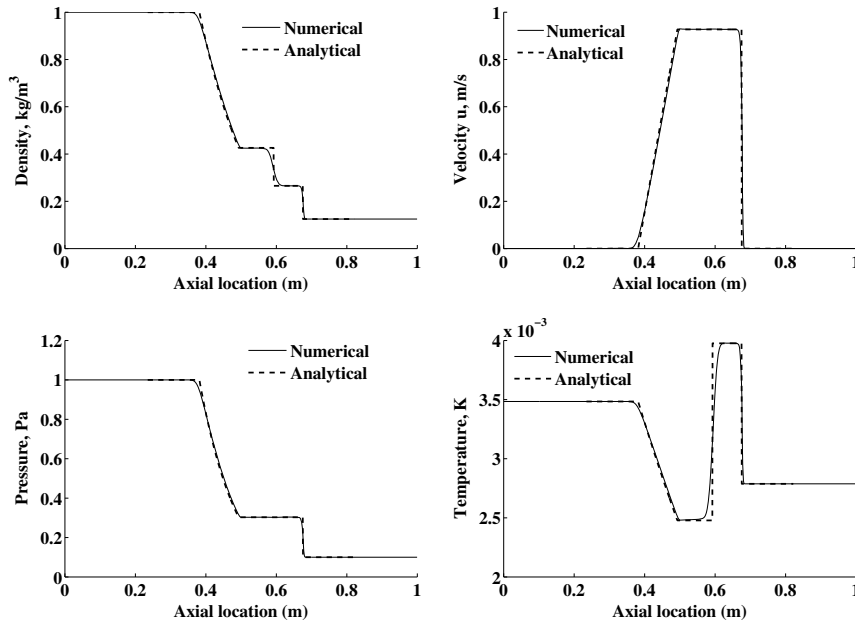
Fig. 4 Comparison between analytical and numerical predictions for a nonrotating shock tube problem after 0.1 s [17].

spanwise velocity inside the duct will be of the order of the duct tip speed

$$\Delta t = 0.3 \frac{\Delta x}{\Omega R} \tag{28}$$

III. Validation of the Numerical Model

The methodology described above was first validated by comparing the output of the numerical model to the analytical solution of a nonrotating shock tube problem. Then, a grid convergence study was performed on the nonrotating shock tube problem as well as on the computed spanwise pressure distribution in a rotating straight duct that was open at both ends. Finally, the output of the numerical model was compared with predictions from a commercial CFD solver (Fluent) for the case of the rotating straight duct that was open at both ends.

A. Nonrotating Shock Tube Problem

A nonrotating shock tube problem, described by Sod [17], was used to validate the numerical model. The setup consists of a 1-m-long tube filled with air. In the initial state, air in the left half of the tube has a density $\rho_L = 1$ kg/m³, pressure $P_L = 1$ Pa, and velocity $u_L = 0$ m/s, while the air in the right half of the tube has a density $\rho_R = 0.125$ kg/m³, pressure $P_R = 0.1$ Pa, and velocity $u_R = 0$ m/s. Predictions of density, velocity, pressure, and temperature from the numerical model after 0.1 s were compared with analytical results (see Fig. 4). It can be seen that the numerical model captures the presence of a shock very well and shows good agreement with analytical results. This shock-capturing ability demonstrates the low numerical dissipation inherent in AUSM.

B. Grid Convergence

The numerical error was compared with the exact solution for the shock tube problem. The total number of cells inside the computational domain was changed from 100 to 6400 keeping all other parameters constant. At time $t = 0.1$ s, the error $(E(x))$ between the exact and numerical solution for pressure can be approximated by

$$E(x) = p(x) - p_{\text{exact}}(x) \approx C(x)h^m \tag{29}$$

Here, h is the grid spacing, m is the order of the leading term in the error, and $C(x)$ is a constant of proportionality for a given spatial

location x. The cumulative error was obtained by averaging the L^2 norm of error obtained at all "N" grid points [Eq. (30)]

$$\|E\|^2 = \frac{1}{N}\sqrt{\sum_{x=0}^{x=L} E(x)^2} = \frac{h^m}{N}\sqrt{\sum_{x=0}^{x=L} C(x)^2} \tag{30}$$

Taking the logarithm of both sides, the above equation becomes

$$\log(E) = \log(K) + m\log(h) \tag{31}$$

where K is an effective proportionality constant. This error is shown in Fig. 5. From a linear fit, the order of convergence (slope) is 0.58. Note that this is lower than the theoretical slope of 1.0 for a first-order upwind scheme. This is because there are additional errors introduced due to time stepping, boundary condition estimation, and the weighted sum L^2 error computation. However, the results show a consistent decrease in error with grid refinement.

Flow through a rotating straight duct open at both ends was studied to demonstrate grid independence of the computed results. The duct parameters chosen for this study are outlined in Table 1.

The steady-state spanwise pressure distribution was computed for 10, 60, and 260 cells in the computational domain (Fig. 6). It can be seen that there is minimal change in the computed pressure distribution for all the three cases. Therefore, it can be concluded that 60 cells in the computational domain are sufficient to obtain a converged solution for the rotating duct.

The results from the current numerical model were compared with results from a 3-D Fluent steady-state simulation for the same parameters as in Table 1. Approximately 500,000 cells were used to represent the rotating duct in the Fluent simulation, while only 60 cells were used to represent the duct in the current quasi 1-D numerical model. A comparison of both computed spanwise pressure distributions is shown in Fig. 7.

It is observed that the quasi 1-D results under predict pressure in the inboard regions of the duct compared with the Fluent simulation. This discrepancy can be attributed to the difference in the viscous force representation between the two solutions. Near the inlet, the viscous forces are comparable to centrifugal forces. Therefore, the difference between a Fanning factor-based viscous force estimation and a full 3-D treatment of viscous fluxes is more pronounced near the inlet. However, in the outboard regions, spanwise pressure is dominated by centrifugal forces and both the solutions capture this effect equally well. It is important to note that the computational time
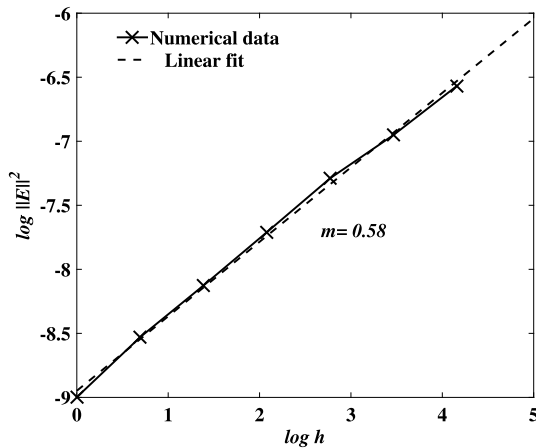
Fig. 5   Dependence of the logarithm of L^2 norm of error on the logarithm of grid spacing h.

taken by the Fluent simulation was approximately 9 hours, while the quasi 1-D code took approximately 4 minutes to produce the steady-state results.

IV.   Results and Discussion

The quasi 1-D numerical model was used to study the flow through a rotating duct with open ends. Note that a typical modern helicopter rotor has a hover tip speed of around 200 m/s; therefore, the flow through the duct for tip speeds around this value is explored. First, the effect of inlet plenum pressure on inviscid flow through the rotating duct is explored; all subsequent discussions focus only on centrifugally pumped flow, that is, with inlet plenum pressure equal to atmospheric pressure. The effect of duct tip speed is then discussed, followed by the effect of friction on the flow. Then, the effect of a flow control valve with time-varying area at different spanwise locations is explored. Finally, the effect of duct sweep is explored. The parameters used in all these computations are listed in Table 2. An internal surface roughness representative of an extruded Aluminum tube was chosen for computation of the Fanning friction factor [Eq. (22a)].

A.   Effect of Inlet Plenum Pressure

The effect of inlet plenum pressure in the inviscid case was explored by varying the duct inlet stagnation pressure P_{stag} from P_{atm} to 1.5 P_{atm} at a tip speed of 183 m/s. The steady-state spanwise duct pressure is plotted in Fig. 8 for different inlet stagnation pressures. Note that, at $t = 0$, the duct instantaneously begins to spin at the specified tip speed and the solution reaches steady state after approximately two revolutions. It can be seen that, when the inlet stagnation pressure P_{stag} is increased to 1.2 P_{atm}, the inlet static pressure decreases and a shock is formed inside the duct (at $x/R \sim 0.8$) to obtain the necessary pressure recovery to match the exit boundary condition (ambient atmospheric pressure). Upon further increasing the inlet stagnation pressure to 1.5 P_{atm}, the shock disappears and the flow is supersonic everywhere. Note that, in this

Table 1   Duct parameters used in grid independence study

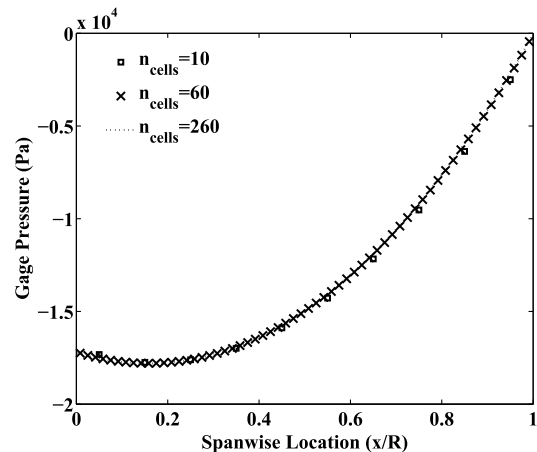|	
Duct length (rotor radius R)	1.32 m
Tip speed	183 m/s
Number of spanwise elements	10, 60, and 260
Duct cross-sectional area	2.165×10^{-3} m^2
Duct sweep	0
Boundary conditions	Open inlet, open outlet
Surface roughness (ϵ)	1.5×10^{-6} m
Courant–Friedrichs–Lewy number	0.7
P_{atm}	101,360 Pa
ρ_{atm}	1.225 kg/m^3
T_{atm}	287 K
K (thermal conductivity of air)	0.028 W/(m · K)

Fig. 6   Comparison of spanwise pressure for different number of cells in the computational domain for a duct spinning at a tip speed of 183 m/s.
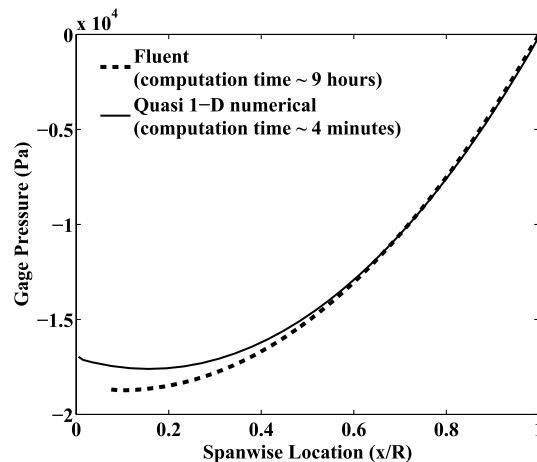

Fig. 7   Comparison between spanwise pressure distribution computed by the quasi 1-D numerical model and by Fluent.

case, the exit pressure does not match ambient atmospheric pressure. The recovery of local pressure to ambient would take place outside the exit, through a series of shocks.

A considerable spanwise pressure rise is seen even with $P_{stag} = P_{atm}$, that is, due to centrifugal pumping alone. Therefore, the remainder of this discussion will focus only on centrifugal pumping, where the duct inlet is exposed to ambient atmospheric conditions.

B.   Effect of Duct Tip Speed

The effect of duct tip speeds of 31, 183, and 213 m/s was studied in the inviscid case, with both the inlet and the outlet open to ambient atmospheric conditions. The duct was started instantaneously from rest and the evolution of duct flow with time was observed. The results can be divided into purely subsonic flow and supersonic flow cases.

Table 2   Duct parameters used in this study

|	
Duct length (rotor radius R)	2 m
Tip speed	31, 183, and 213 m/s
Courant–Friedrichs–Lewy number	0.3
Number of spanwise elements	60
Duct area	3.125×10^{-3} m^2
Duct sweep	0, 30, 60, and 90 deg
Surface roughness (ϵ)	1.5×10^{-6} m
Ambient atmospheric pressure P_{atm}	101,360 Pa
Ambient atmospheric density ρ_{atm}	1.225 kg/m^3
Ambient atmospheric temperature T_{atm}	287 K
K (thermal conductivity of air)	0.028 W/(m · K)
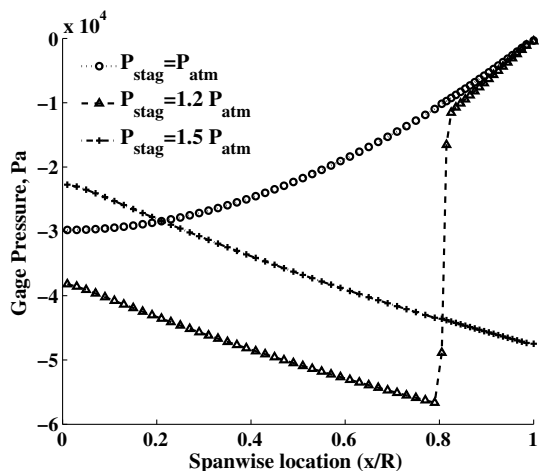
Fig. 8 Effect of inlet stagnation pressure P_{stag} on steady-state spanwise pressure distribution. Inviscid case, duct tip speed = 183 m/s.

1. Subsonic Internal Flow

At a low tip speed corresponding to near-incompressible flow, it can be analytically shown for inviscid flow that the internal flow velocity is the same as the tip speed ($u_{\text{axial}} = V_{\text{tip}} = \Omega R$) [18]. This result can be seen in Fig. 9 for the duct tip speed of 31 m/s. After 1.2 rotor revolutions, the spanwise velocity settles to a constant value of approximately 31 m/s (equal to the tip speed), all along the duct. Pressure increases monotonically with radial location such that the gradient of pressure distribution equals the centrifugal force.

At higher tip speeds, the effect of compressibility becomes apparent. At a duct tip speed of 183 m/s (Fig. 10), there are large spanwise variations in flow features. The density, pressure, and temperature at the duct exit are equal to their ambient atmospheric values. At the open inlet, density, pressure, and temperature are observed to be much lower than ambient values. The duct flow reaches steady state after 1.8 revolutions. The spanwise velocity is maximum at the root of the duct and monotonically decreases toward the tip due to compressibility.

2. Supersonic Internal Flow

As the duct spins at higher rotational speeds, the internal flow velocity increases and eventually becomes supersonic. Figure 11 shows the density, velocity, pressure, and temperature inside the duct rotating at a tip speed of 213 m/s. Initially, the flow is subsonic along

the duct; however, a shock begins to form after 1.2 revolutions, and is well developed at $x/R \sim 0.6$ after 2.4 revolutions. Note that the exit boundary values of density, pressure, and temperature are equal to the ambient atmospheric conditions.

It is interesting to observe the evolution of the shock over a longer time scale. The shock stays at the same spanwise location from two to eight rotor revolutions. However, as shown in Fig. 12, the shock moves inboard from 8.5 revolutions to 17 revolutions, and eventually exits the duct through the inlet. The flow is isentropic inside the duct between 17.3 and 18.0 revolutions, after which the shock reappears at its original location (at 18.7 revolutions), moves slightly outboard at 20.4 revolutions, and then moves toward the inlet. This shock movement is periodic, with a time period of approximately 17.5 rotor revolutions.

Figure 13 shows the torque due to internal flow for the three tip speeds (31, 183, and 213 m/s). Zero rotor torque corresponds to no flow through the duct. It can be seen that, with an increase in tip speed, the required rotor torque increases. For subsonic internal flow, the torque is constant; however, for the supersonic internal flow case, there are periodic oscillations in torque due to the movement of the shock in the duct.

C. Effect of Friction

In reality, viscosity of the air causes energy dissipation and results in a lower duct velocity than predicted in the inviscid case. Viscous effects in the quasi 1-D numerical model are incorporated using a friction factor. For a tip speed of 183 m/s, the flow remains subsonic in the duct (Fig. 14), and the maximum duct velocity is substantially lower than in the inviscid case (Fig. 10). Furthermore, in contrast to the inviscid case, spanwise pressure does not increase monotonically. A drop in spanwise pressure is observed for $x/R < 0.2$. This is because, near the inlet, the centrifugal force is much smaller than the friction force. Therefore, to obtain a static force balance in steady flow, the spanwise pressure differential becomes negative. However, beyond $x/R = 0.2$, the centrifugal force dominates, and the spanwise pressure differential increases to restore force balance. The same trend is seen in the spanwise temperature and density.

At a tip speed of 213 m/s (Fig. 15), in contrast to the inviscid case, no shock is formed. It was observed that, due to duct friction, a shock formed only when the duct tip speed was greater than 260 m/s, which is unrealistic for a helicopter rotor. The effect of the shock can be seen in terms of the mass flow rate through the duct, as shown in Fig. 16. A significant difference in mass flow rate is observed between the inviscid duct flow and the case with duct friction. Above
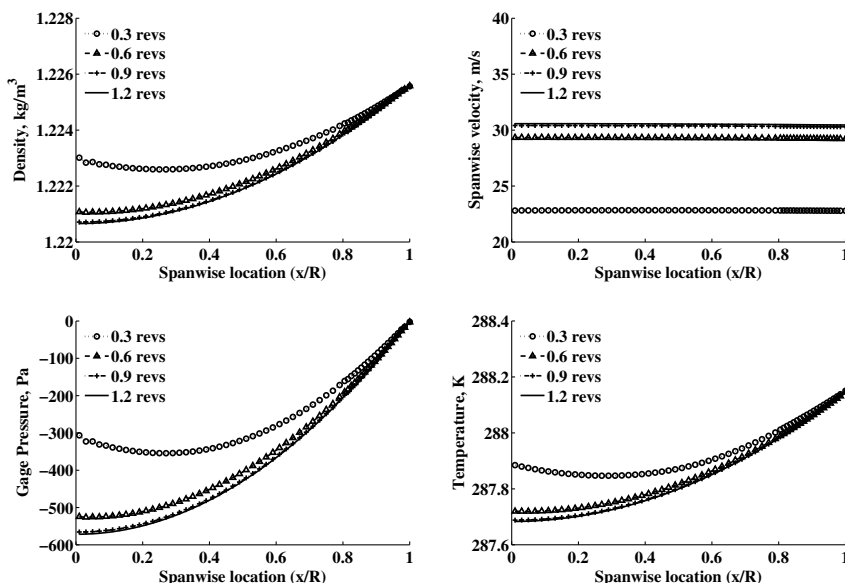

Fig. 9 Computed spanwise density, velocity, pressure, and temperature for inviscid flow through a duct spinning at a tip speed of 31 m/s with an open inlet and open outlet.
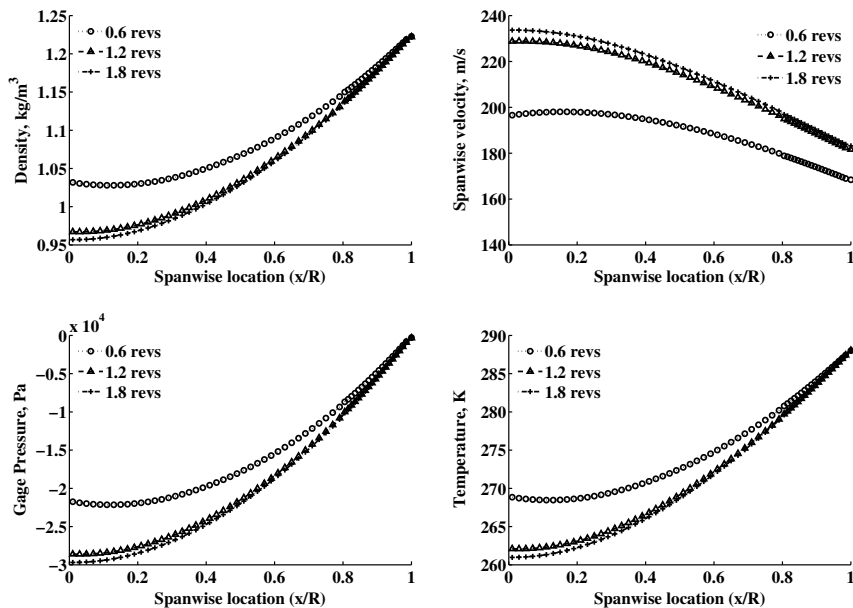
Fig. 10   Computed spanwise density, velocity, pressure, and temperature for inviscid flow through a duct spinning at a tip speed of 183 m∕s with an open inlet and open outlet.

a certain tip speed, a shock is formed inside the duct, the flow becomes choked, and the mass flow rate becomes a constant.

D.   Duct Flow Control Valve

The effect of a flow control valve with a time-varying cross-sectional area on the internal flow was studied at a tip speed of 183 m/s, including duct friction. The valve was closed until approximately 7.3 rotor revolutions, after which it was instantaneously opened. The duct flow was computed for three valve locations, given by $x_{valve} = 0$, $x_{valve} = 0.5R$, and $x_{valve} = R$.

1.   Valve at $x_{valve} = 0$

A valve was located at the inlet of the duct and was suddenly opened at 7.3 revolutions. Figure 17 shows the duct pressure at four spanwise locations ($x = 0$, $x = R/3$, $x = R/2$, $x = R$). Initially, when the valve is closed, there are periodic oscillations in pressure at all four stations. These oscillations occur at a frequency of around

43 Hz, which is equal to the fundamental frequency of a 2 m duct closed at one end. Furthermore, the amplitude of oscillations decreases closer to the exit, with minimal oscillations present at the exit. As soon as the valve opens, a sudden increase in duct pressure occurs at $x = 0$, $x = R/3$ and $x = R/2$. However, this soon decays due to the large convective flux, that is, large mass flow rate of air through the duct. The pressure at $x = R$ settles to the ambient atmospheric pressure value, while the inlet pressure settles to a value much lower than ambient pressure, as governed by the boundary conditions.

The duct velocity along the span is shown in Fig. 18. When the valve is closed, there are oscillations in duct velocity occurring at the natural frequency of the duct. The amplitude of oscillations is largest near the exit and it becomes vanishingly small near the duct inlet, that is, closed valve. Once the valve is opened, the oscillations in velocity decay rapidly and a steady-state value is reached, the magnitude of which decreases along the duct.
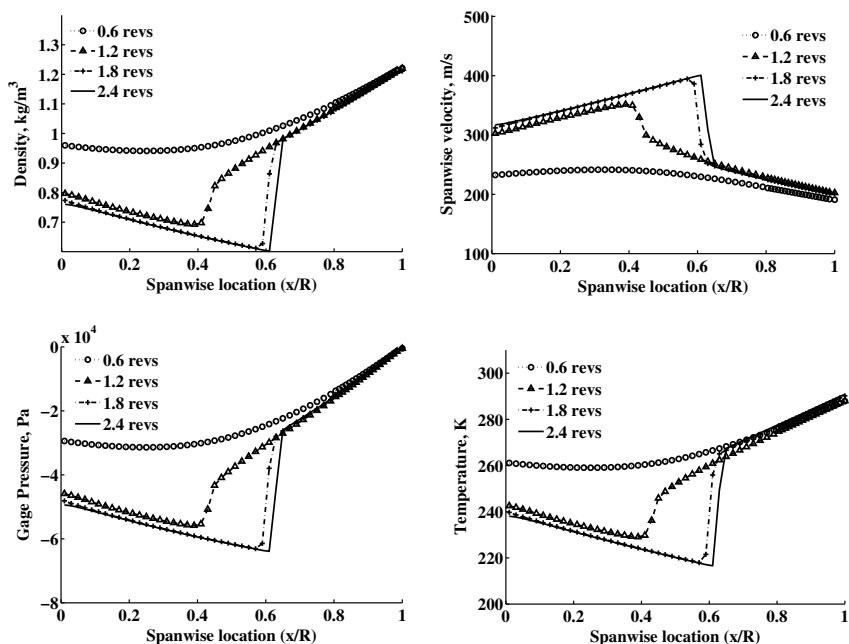

Fig. 11   Computed inviscid flow through a duct spinning at a tip speed of 213 m∕s with an open inlet and open outlet.
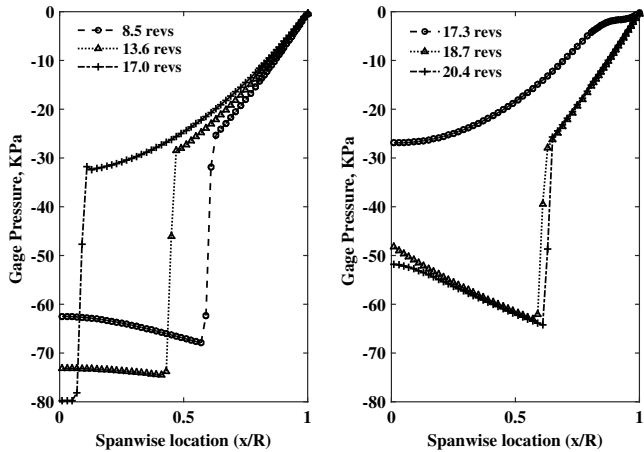
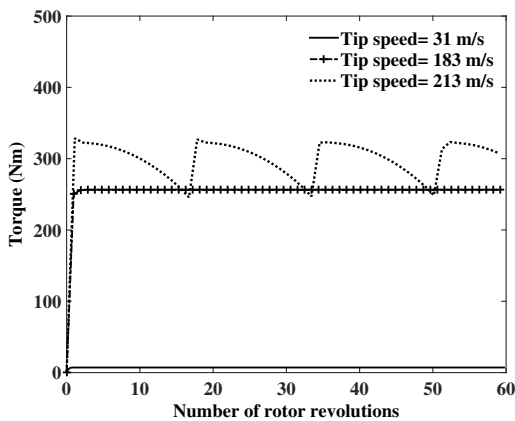Fig. 12 Computed results (inviscid flow) showing the motion of the internal shock with time.

Fig. 13 Computed torque for inviscid flow through a duct with open inlet and open outlet, rotating at tip speeds of 31, 183, and 213 m/s.

natural frequency of a 1-m-long duct. The pressure oscillations are seen to have the largest amplitude at the midpoint of the duct (where the valve is located) and diminish near the inlet and outlet of the duct. Moreover, even when the valve is closed, all the oscillations decayed rapidly (within five rotor revolutions). Once the valve is opened, pressure quickly attains its steady-state value, while the outlet pressure is equal to the ambient atmospheric pressure.

3. Valve at $x_{\text{valve}} = R$

Figure 20 shows the duct pressure for a valve located at $x_{\text{valve}} = R$, opened instantaneously at 7.3 revolutions. When the valve is closed, there are pressure oscillations at all spanwise stations. The frequency of these oscillations is 41 Hz, which is close to the natural frequency of the duct (~43 Hz). The amplitude of oscillations is maximum at the outlet (closed valve) and decreases closer to the inlet (ambient pressure). When the valve opens, the pressure at all spanwise locations settles rapidly after a small time lag, which corresponds to the time it takes for the information (of valve opening) to propagate from the outlet to other locations in the duct. Note that the pressure at the outlet is equal to ambient atmospheric pressure, as governed by the exit boundary conditions.

4. Hub Forces

The hub spanwise force (F_x) and chordwise force (F_y) due to internal flow corresponding to different valve locations are shown in Fig. 21. The spanwise force represents the sum of duct friction and pressure acting on the valve, while the chordwise force represents the Coriolis force acting along the span of the duct. Note that the magnitude and phasing of F_y is important for stability in the lead-lag degree of freedom.

When the valve is closed, periodic oscillations in F_x and F_y are seen, corresponding to the natural frequency of the duct. These oscillations are larger in magnitude when the valve is located either at the inlet or at the outlet. The mean spanwise force is largest when the valve is at the outlet and is minimum when the valve is at the inlet. This is because when the valve is at the outlet ($x_{\text{valve}} = R$), the spanwise pressure force acting on the valve is in the same direction as the friction force on the duct. However, when the valve is at the inlet ($x_{\text{valve}} = 0$), the pressure on the valve opposes duct friction, reducing the net spanwise force. In both these cases, the frequency of oscillations is close to the natural frequency of the duct (~43 Hz). When the valve is located in the middle of the duct $x_{\text{valve}} = 0.5R$, nonperiodic fluctuations are observed, which could be attributed to the fact that there are two ducts in contact with each other at the valve: an open-closed duct inboard and a closed-open duct outboard. Therefore, the combined effect of pressure oscillations in the two halves of the duct results in nonperiodic spanwise and chordwise force fluctuations. However, as soon as the valve is opened, the

2. Valve at $x_{\text{valve}} = 0.5R$

For a valve located at $x_{\text{valve}} = 0.5R$ (see Fig. 19), when it is closed, the inboard half of the duct behaves as an open-closed duct, while the outboard half behaves as a closed-open duct. During this time, it can be seen that there are periodic oscillations in spanwise pressure, occurring at approximately 73 Hz, which is higher than the natural frequency of a 2-m-long duct closed at one end, but is lower than the
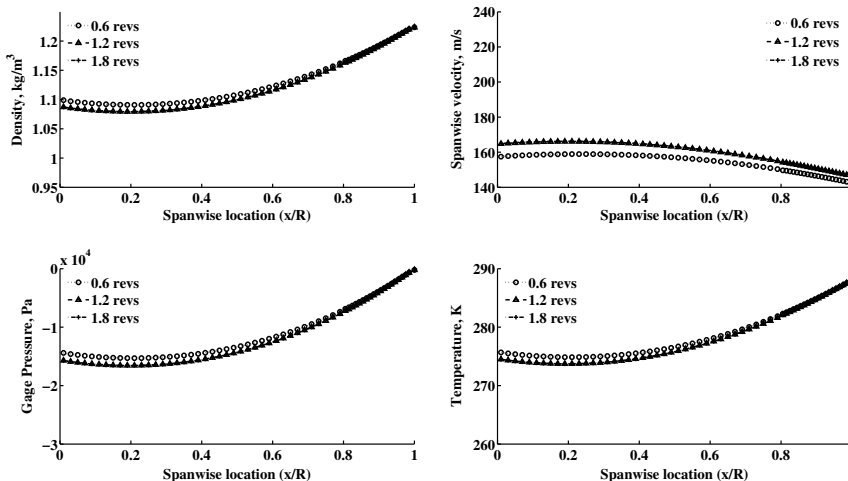

Fig. 14 Density, velocity, pressure, and temperature inside a duct with friction, with open inlet and open outlet, spinning at a tip speed of 183 m/s.
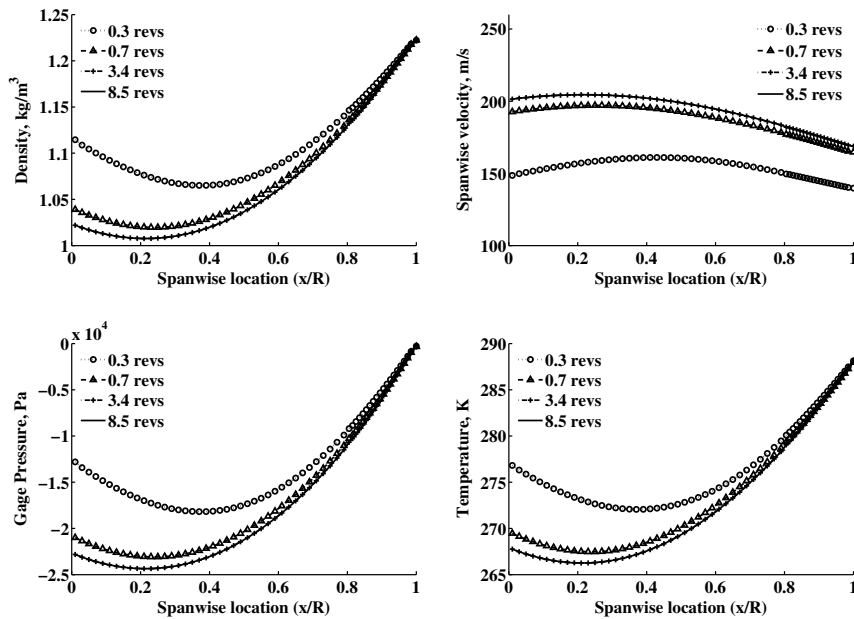
Fig. 15   Density, velocity, pressure, and temperature inside a duct with friction, with open inlet and open outlet, spinning at a tip speed of 213 m/s.
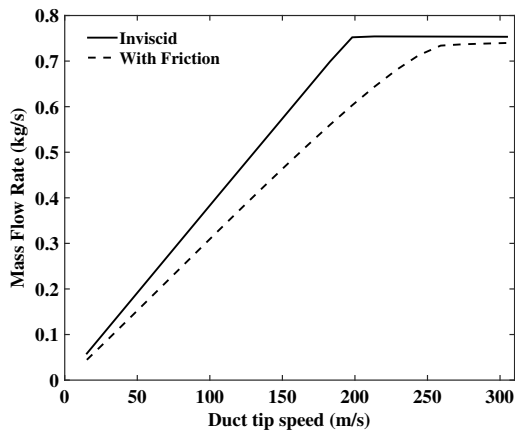

Fig. 16   Mass flow rate of air in a rotating duct with open inlet and open outlet, comparison between inviscid case and duct with friction.

spanwise and chordwise forces quickly attain a constant value for all the three cases.

It can be concluded that the location of the valve plays a significant role in the phasing and transient response of duct pressure, and therefore the spanwise and chordwise force on the hub. In a rotor blade with internal flow, this can have an effect not only on lead-lag stability but also on the transient dynamics of on-blade actuators, CC, or other devices driven by the centrifugal pumping. From a practical point of view, it is easiest to incorporate a flow control valve near the rotor hub, where the centrifugal forces are lower and space constraints are less severe than at outboard locations on the rotor blade. Therefore, the quasi 1-D numerical model can also be used in the design of actuation schemes relying on centrifugal pumping.

E. Effect of Duct Sweep

The effect of duct sweep angle (0, 30, 60, and 90 deg) on the total rotor torque was explored. The duct was assumed to be straight up to $x/R = 0.8$, beyond which, the duct is swept. The radius of curvature
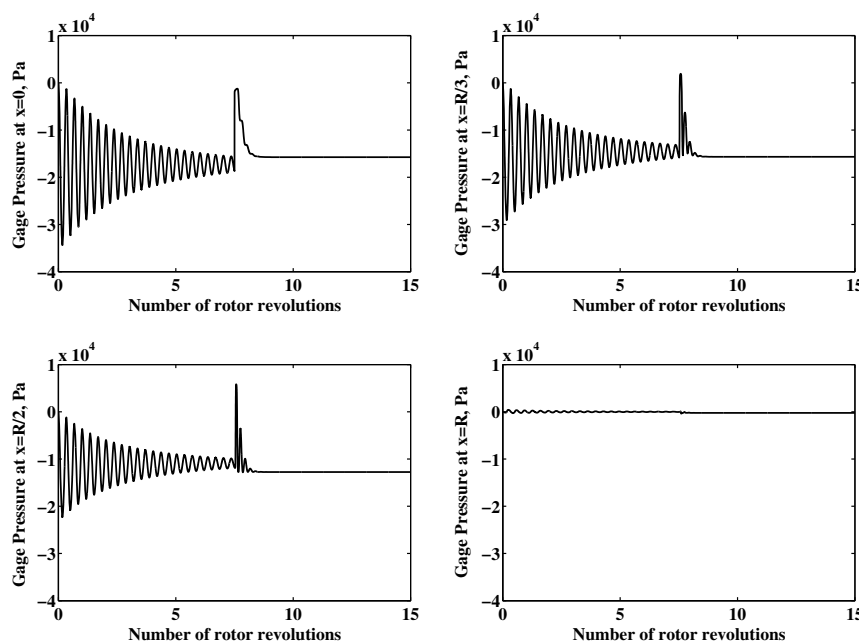

Fig. 17   Duct pressure at spanwise locations $x = 0$, $x = R/3$, $x = R/2$, $x = R$, when the valve is located at $x_{valve} = 0$.
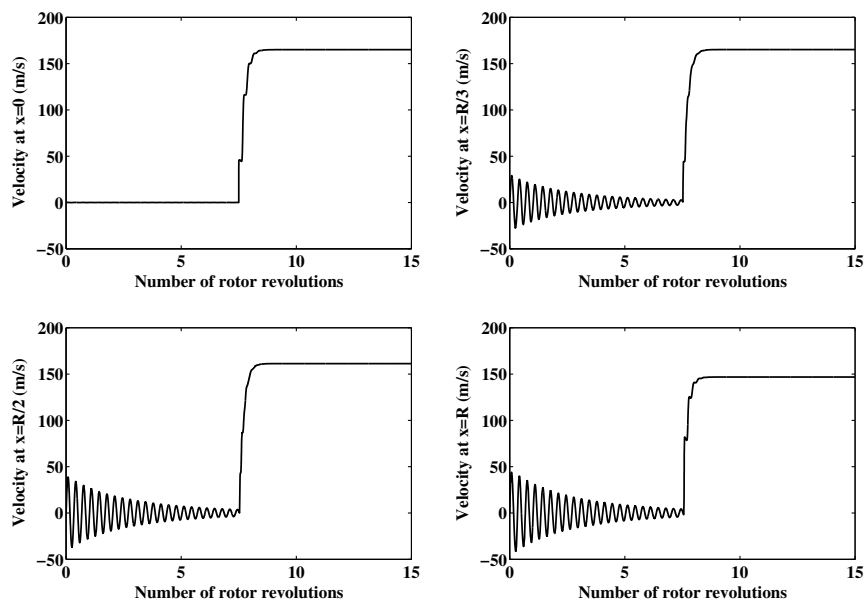
Fig. 18   Duct velocity at spanwise locations $x = 0$, $x = R/3$, $x = R/2$, $x = R$, when the valve is located at $x_{\mathrm{valve}} = 0$.

of the transitional region is taken to be $0.2R$. A nominal tip speed of 183 m/s was chosen for all the cases, to represent a compressible subsonic flow case. The total rotor torque depends on the magnitude of efflux velocity perpendicular to the span of the duct. As the aft sweep angle increases, the momentum of flow exiting the duct acts in the direction of rotation, thereby reducing rotor torque. At $\theta = 90$ deg, the entire flow exits the duct perpendicular to the span of the duct and the total rotor torque is minimum. The rotor torque for different values of sweep is shown in Fig. 22. These values of rotor torque were obtained after 1.5 revolutions of the duct, when internal flow had reached steady state. Rotor torque shows a decreasing trend with an increase in sweep angle. For a 30 deg sweep, typical in helicopter blades, the torque predicted was 131 N · m, which was 36% lower than the torque for the unswept case (205 N · m). When the sweep angle is 90°, it is seen that the rotor torque is ∼38 N · m. This residual torque is due to the addition of a small duct extension (∼0.02 m) close to the exit. However, the general trend of torque diminishing with duct sweep angle is well captured by the analysis.

V.   Conclusions

A quasi 1-D numerical model was developed to compute the internal flow inside a rotating duct. The model solves the Euler equations using a finite volume formulation with inviscid fluxes calculated using the advection upwind splitting method. Centrifugal and Coriolis effects, duct friction, time-dependent boundary conditions, duct sweep, and a spanwise flow control valve are included. The model was validated by computing the flow through a rotating duct with open ends, and comparing it with the results from a commercial computational fluid dynamics (CFD) solver. Significant savings in computational time were observed; the solution required approximately 4 minutes in the quasi 1-D model and approximately 9 hours in the commercial CFD solver. Therefore, the quasi 1-D model can be used as a fast design tool for rotors and on-blade actuators relying on centrifugal pumping.

The quasi 1-D model was used to compute the flow inside a 2-m-long rotating duct with open ends, and to evaluate the effect of inlet plenum pressure, duct rotational speed, duct friction, a flow control
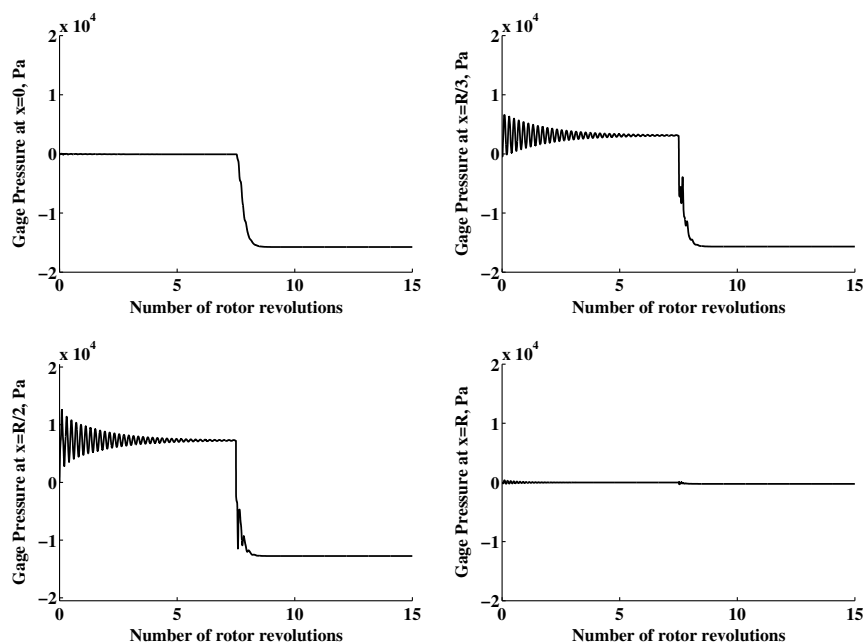

Fig. 19   Duct pressure at spanwise locations $x = 0$, $x = R/3$, $x = R/2$, $x = R$, when the valve is located at $x_{\mathrm{valve}} = 0.5R$.
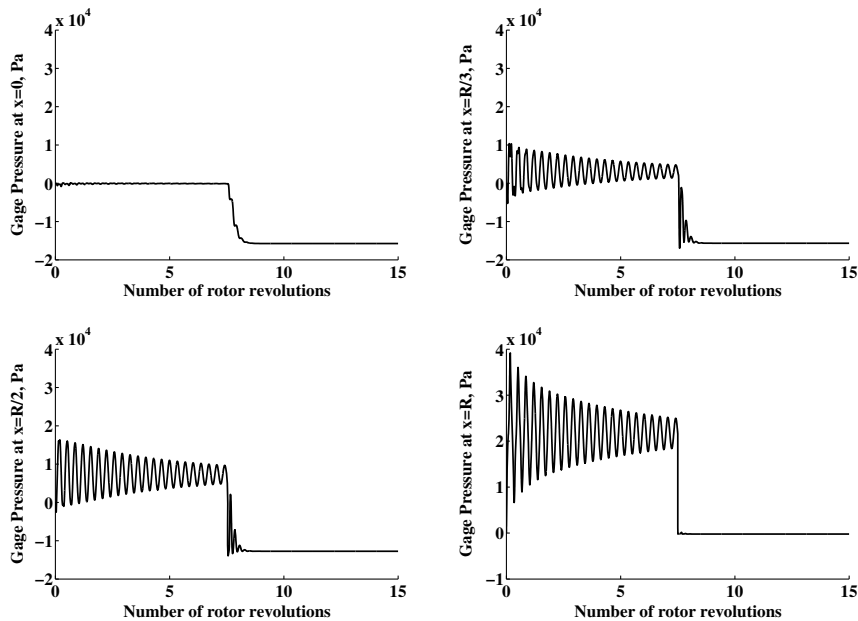
Fig. 20   Duct pressure at spanwise locations $x = 0, x = R/3, x = R/2, x = R$, when the valve is located at $x_{valve} = R$.
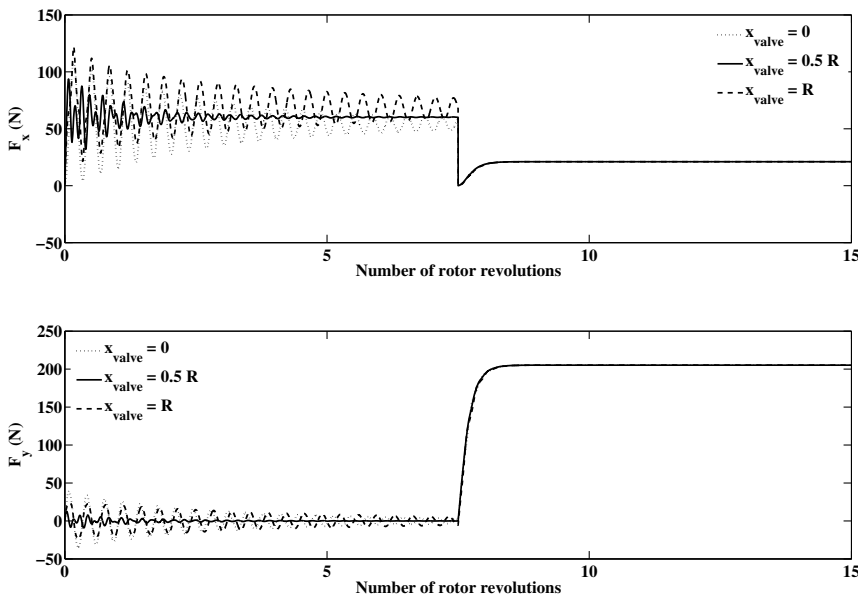

Fig. 21   Net spanwise and chordwise force as a function of time for different valve locations.
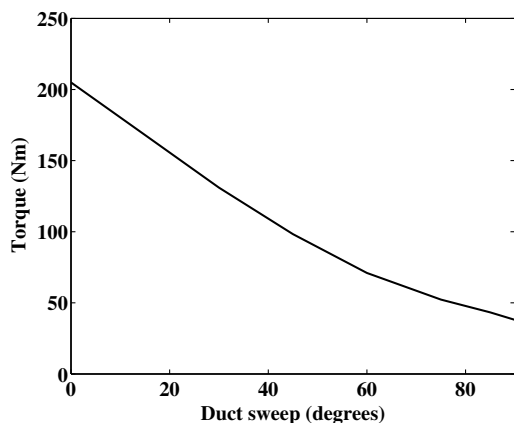

Fig. 22   Effect of duct sweep angle on rotor torque.

valve at several spanwise locations opening instantaneously, and duct sweep. Several interesting phenomena were observed. With an inlet stagnation pressure of 1.5 times atmospheric, a shock forms in the duct at a tip speed of 183 m/s; note that the hover tip speed of a typical helicopter rotor is in the range 190–215 m/s. All subsequent results were obtained for centrifugal pumping alone, that is, with the inlet stagnation pressure equal to ambient atmospheric pressure.

The duct velocity at low subsonic tip speed was almost constant spanwise, and equal to the tip speed; this is also predicted by the exact analytical solution. At higher tip speeds, the duct velocity decreases along the span due to compressibility. In the inviscid case, at a duct tip speed of 213 m/s, a shock forms inside the duct and moves inboard, exiting the duct through the inlet and reappearing inside the duct at an outboard location. This periodic motion occurs with a time period of approximately 17.5 rotor revolutions, and also results in a periodic oscillations in rotor torque. However, with duct friction included, the shock does not exhibit periodic motion and only appears at a tip speed of 260 m/s, which is much higher than the tip speed of a realistic

helicopter rotor. This indicates that choking of the internal flow may not be an issue for a practical helicopter rotor blade with centrifugal pumping.

A closed flow control valve along the rotating duct produces oscillations in hub spanwise forces and rotor torque, which are maximum when the valve was placed either at the duct inlet or at the duct outlet. The amplitude of pressure fluctuations decreases with distance from a closed valve inside the duct. Therefore, in applications requiring flow control, a careful trade study of the valve position is necessary to obtain the desired phasing of pressure and velocity with azimuthal angle. Aft duct sweep is beneficial in terms of reducing required rotor torque; this dependence is nonlinear. For example, a typical rotor with a 30 deg aft sweep results in a torque reduction of around 36%.

In the present study, the static pressure at the duct exit was specified equal to ambient atmospheric pressure. It is also possible to obtain more accurate results by coupling the quasi 1-D model to an external flow solver; in this case, the duct exit static pressure would be computed iteratively, that is, specified by the external flow solver at each iteration.

Acknowledgments

References

[1] Krauss, T. A., and Kingston, L., *X-Wing Aircraft Circulation Control*, U.S. Patent 4,573,871, 1986.

[2] Mitchell, C. A., and Vogel, B. J., "The Canard Rotor Wing (CRW) Aircraft—A New Way to Fly," *AIAA/ICAS International Air and Space Symposium and Exposition: The Next 100 Years*, AIAA Paper 2003-2517, July 2003.

[3] Szefi, J., Cormier, B., and Ionno, L., "Full-Scale Experimental Validation of Dynamic, Centrifugally Powered Pneumatic Actuators for Active Rotor Blade Surfaces," *70th Annual Forum*, AHS, Montreal, May 2014.

[4] Drury, M., Szefi, J., and Palacios, J., "Full-Scale Testing of a Centrifugally Powered Pneumatic Deicing System for Helicopter Rotor Blades," *71st Annual Forum*, AHS, Virginia Beach, VA, May 2015.

[5] Johnston, J. P., Halleent, R. M., and Lezius, D. K., "Effects of Spanwise Rotation on the Structure of Two-Dimensional Fully Developed Turbulent Channel Flow," *Journal of Fluid Mechanics*, Vol. 54, No. 1, 1972, pp. 533–557.
doi:10.1017/S0022112072002502

[6] Iaccarino, G., Ooi, A., Reif, B. A. P., and Durbin, P., "RANS Simulations of Rotating Flows," *Center of Turbulence Research, Annual Research Briefs*, 1999, pp. 257–266.

[7] Li, B., Liu, N., and Lu, X., "Direct Numerical Simulation of Wall-Normal Rotating Turbulent Channel Flow with Heat Transfer," *International Journal of Heat and Mass Transfer*, Vol. 49, No. 5, 2006, pp. 1162–1175.
doi:10.1016/j.ijheatmasstransfer.2005.08.030

[8] Liu, N., and Lu, X., "A Numerical Investigation of Turbulent Flows in a Spanwise Rotating Channel," *Computers & Fluids*, Vol. 36, No. 2, 2007, pp. 282–298.
doi:10.1016/j.compfluid.2005.11.004

[9] Williams, R. M., "Analysis of the Hover Performance of a High Speed Circulation Control Rotor," Naval Ship Research and Development Center Technical Note AL-221, Bethesda, MD, Aug. 1971.

[10] Tongchitpakdee, C., Benjanirat, S., and Sankar, L. N., "Numerical Studies of the Effects of Active and Passive Circulation Enhancement Concepts on Wind Turbine Performance," *Journal of Solar Energy Engineering*, Vol. 128, No. 4, 2006, pp. 432–444.
doi:10.1115/1.2346704

[11] Watkins, C. B., Dutta, S. K., and Reader, K. R., "Numerical and Experimental Simulation of Circulation Control Rotor Pneumodynamics," *AIAA Aircraft Design, Systems and Technology Meeting*, AIAA, New York, 1983.

[12] Watkins, C. B., Reader, K. R., and Dutta, S. K., "Pneumodynamic Characteristics of a Circulation Control Rotor Model," *Journal of the American Helicopter Society*, Vol. 30, No. 1, 1985, pp. 23–31.
doi:10.4050/JAHS.30.23

[13] Chopra, I., "Dynamic Stability of a Bearingless Circulation Control Rotor Blade in Hover," *Journal of the American Helicopter Society*, Vol. 30, No. 4, 1985, pp. 40–47.
doi:10.4050/JAHS.30.40

[14] Liou, M., and Steffen, C. J. Jr, "A New Flux Splitting Scheme," *Journal of Computational Physics*, Vol. 107, No. 1, 1993, pp. 23–39.
doi:10.1006/jcph.1993.1122

[15] Hirsch, C., *Numerical Computation of Internal and External Flows: The Fundamentals of Computational Fluid Dynamics*, Vol. 1, Butterworth-Heinemann, Oxford, 2007.

[16] Churchill, S. W., "Friction-Factor Equation Spans All Fluid-Flow Regimes," *Chemical Engineering*, Vol. 84, No. 24, 1977, pp. 91–92.

[17] Sod, G. A., "A Survey of Several Finite Difference Methods for Systems of Nonlinear Hyperbolic Conservation Laws," *Journal of Computational Physics*, Vol. 27, No. 1, 1978, pp. 1–31.
doi:10.1016/0021-9991(78)90023-2

[18] Tonon, D., Nakiboglu, G., Golliard, J., and Hirschberg, A., "Voice of the Dragon: The Mystery of the Missing Fundamental Mode," *Proceedings of the 20th International Symposium on Music Acoustics*, Sydney, Katoomba, Australia, Aug. 2010.

A. Lyrintzis
Associate Editor